Available online at www.sciencedirect.com
SCIENCE DIRECT®
Journal of Magnetic Resonance 172 (2005) 214–221
JMR Journal of Magnetic Resonance
www.elsevier.com/locate/jmr

^{2}H $T_{2\rho}$ relaxation dynamics and double-quantum filtered NMR studies

Dennis W. Hwang*, Wei-Jie Jhao, Lian-Pin Hwang

Department of Chemistry, National Taiwan University, Taipei, Taiwan, ROC
Institute of Atomic and Molecular Sciences, Academia Sinica, Taipei, Taiwan, ROC

Received 14 May 2004; revised 15 October 2004
Available online 21 November 2004

Abstract

In this study ^{2}H $T_{2\rho}$ DQF NMR spectra of water in MCM-41 were measured. The $T_{2\rho}$ double-quantum filtered (DQF) NMR signal is generated by applying a radio frequency (RF) field for various durations and then observed after a monitor RF pulse. It was found that the transfer between different quantum coherences by the couplings during long-duration RF fields (i.e., soft pulses) and that residual quadrupolar interaction dominates the signal decay. Knowledge of coherence transfer during long-RF pulses has special significance for the development of sophisticated multi-quantum NMR experiments especially multi-quantum MRI applications.

Keywords: $T_{2\rho}$; DQF NMR

1. Introduction

Knowledge of the dynamics of adsorbate molecules is very important for understanding mesoporous materials and catalysts. The dynamics of such molecules is generally slow on the NMR time scale. NMR rotating frame relaxation rate measurements have been used to study the slow motional regime. In developing the theory needed to analyze such experiments, Blicharski [1] considered the quadrupolar relaxation for the spin $I = 1$ system in detail. In a later work, ignoring the effects of spin relaxation, the dynamics of a spin $I = 1$ nuclei system with a static residual quadrupolar interaction under a short pulse irradiation of a radio frequency (RF) field were investigated by Vega and Pines [2]. Conventional double-quantum filtered (DQF) NMR spectroscopy probes residual quadrupolar interactions and it has been used as a diagnostic tool for detecting anisotropic adsorption interactions in porous systems [3–5]. The effects of the residual quadrupolar interaction and the associated relaxation mechanisms on DQF NMR have been analyzed by Jacobsen et al. [6] and Van der Maarel [7].

The aim of the present study is to demonstrate a more sophisticated variant of conventional DQF NMR, the $T_{2\rho}$ double-quantum filtered (DQF) experiment. We studied the evolution of the relevant spin tensor operator describing the effects of long-duration RF fields (i.e., 'soft pulses') on the residual quadrupolar interaction resulting from adsorption. The theory developed in this work is useful for understanding the coherence-transfer pathway among different spin multi-poles, and in the development of sophisticated RF soft pulses for multi-quantum magnetic resonance imaging [8,9].

2. Theory

The spin system evolves under the simultaneous action of the Zeeman, residual quadrupolar interaction,

* Corresponding author. Fax: +886 2 33663294.
E-mail address: dwh@gate.sinica.edu.tw (D.W. Hwang).

1090-7807/$ - see front matter © 2004 Elsevier Inc. All rights reserved.
doi:10.1016/j.jmr.2004.10.008

and RF Hamiltonians. Here the residual quadrupolar interaction is defined as a motionally averaged Hamiltonian which is axially symmetric with respect to the principal axis of motion [5–8]

$$\begin{aligned} H_q &= \omega_{q,\theta}(I_z^2 - \tfrac{1}{3}I(I+1)) \\ &\equiv \omega_q(\tfrac{1}{2})(3\cos^2\theta - 1)(I_z^2 - \tfrac{1}{3}I(I+1)), \end{aligned} \tag{1}$$

where θ is the angle between the z-axis of the molecular frame and the Zeeman field. $\omega_{q,\theta}$ and ω_q are the (motionally averaged) residual quadrupolar interactions, defined in the laboratory and the molecular frames, respectively. An isotropic distribution of θ is applied to approximate the location of the adsorption sites under the random orientational distribution in our powder sample.

The RF field is assumed to be exactly on resonance along the x-axis with field strength B_1 and frequency ω_1. Thus the total Hamiltonian expressed in the rotating frame reads:

$$\begin{aligned} H_{\text{total}} &= H_q + H_1 \equiv \omega_{q,\theta}(I_z^2 - \tfrac{1}{3}I(I+1)) + \omega_1 I_x \\ &\equiv \omega_q(\tfrac{1}{2})(3\cos^2\theta - 1)(I_z^2 - \tfrac{1}{3}I(I+1)) + \omega_1 I_x. \end{aligned} \tag{2}$$

In this study, the spin density operators and Hamiltonian are expressed in terms of irreducible tensorial operators. The mth component of a rank l irreducible tensorial component, T_{lm}, can be related to the elements of a common density matrix. The symmetric and antisymmetric combinations of spin irreducible tensor operators [7,10] are defined by

$$\begin{aligned} T_{lm}(s) &\equiv 1/\sqrt{2}(T_{l-m} + T_{lm}), \\ T_{lm}(a) &\equiv 1/\sqrt{2}(T_{l-m} - T_{lm}). \end{aligned} \tag{3}$$

The irreducible tensor operators in Eq. (3) can be expressed in terms of conventional spin operators by

$$\begin{aligned} T_{10} &= I_1, \\ T_{11}(s) &= -\mathrm{i}I_y, \\ T_{11}(a) &= I_x, \\ T_{20} &= \frac{1}{\sqrt{6}}[3I_z^2 - I(I+1)], \\ T_{21}(s) &= \frac{-\mathrm{i}}{\sqrt{2}}(I_zI_y + I_yI_z), \\ T_{21}(a) &= \frac{1}{\sqrt{2}}(I_zI_x + I_xI_z), \\ T_{22}(s) &= \frac{1}{\sqrt{2}}(I_x^2 - I_y^2), \\ T_{22}(a) &= \frac{-\mathrm{i}}{\sqrt{2}}(I_xI_y + I_yI_x). \end{aligned} \tag{4}$$

T_{10}, $T_{11}(a)$, and $T_{11}(s)$ denote the usual longitudinal magnetization, and the components of transverse magnetization along the x- and y-directions, respectively. Eq. (2) may be recast in terms of the tensorial operators

$$H_{\text{total}} = H_q + H_1 \equiv \sqrt{\frac{2}{3}}\omega_{q,\theta}T_{20} + \omega_1 T_{11}(a). \tag{5}$$

The time evolution of the density operator under H_{total} is given by the Liouville equation

$$\frac{\mathrm{d}\sigma(t)}{\mathrm{d}t} = -\mathrm{i}[H_{\text{total}}, \sigma(t)], \tag{6}$$

where $\sigma(t)$ represents the density operator defined in terms of the set of irreducible tensor components [$\hat{T}_{20}$, $\hat{T}_{11}(a)$, $\hat{T}_{21}(s)$, $\hat{T}_{22}(s)$, $\hat{T}_{10}$, $\hat{T}_{11}(s)$, $\hat{T}_{21}(a)$, and $\hat{T}_{22}(a)$]. The evolution of the initial Zeeman order T_{10} evolves through the coupling scheme to $\hat{T}_{11}(s)$, $\hat{T}_{21}(a)$, and $\hat{T}_{22}(a)$. Using the commutation relations [6,7], Eq. (6), in terms of the irreducible tensor component, under the influences of residual quadrupolar interaction, RF field, and spin relaxation [4] becomes

$$\frac{\mathrm{d}}{\mathrm{d}t}\begin{bmatrix} T_{10}^\alpha \\ T_{11}^\alpha(s) \\ T_{21}^\alpha(a) \\ T_{22}^\alpha(a) \end{bmatrix} = \begin{bmatrix} -R_{10}^\alpha & -\mathrm{i}\omega_1 & R_{\omega 1}^\alpha & 0 \\ -\mathrm{i}\omega_1 & -R_{11s}^\alpha & \mathrm{i}\omega_{q,\theta} & 0 \\ 0 & \mathrm{i}\omega_{q,\theta} & -R_{21a}^\alpha & -\mathrm{i}\omega_1 \\ 0 & R_{\omega 1}^\alpha & -\mathrm{i}\omega_1 & -R_{22a}^\alpha \end{bmatrix} \begin{bmatrix} T_{10}^\alpha \\ T_{11}^\alpha(s) \\ T_{21}^\alpha(a) \\ T_{22}^\alpha(a) \end{bmatrix} \equiv R^\alpha \sigma_\alpha, \tag{7}$$

where

$$\begin{aligned} R_{\omega 1}^\alpha &\equiv C^\alpha[3\omega_1\omega_{q,\theta}[J_0^\alpha(0) - J_0^\alpha(k_1)]/k_1^2, \\ R_{10}^\alpha &\equiv C^\alpha[2J_1^\alpha(\omega_0) + 4J_2^\alpha(2\omega_0)], \\ R_{11s}^\alpha &\equiv C^\alpha\{3[\omega_{q,\theta}^2 J_0^\alpha(0) + 2\omega_1^2(J_0^\alpha(0) + J_0^\alpha(k_1))]/k_1^2 \\ &\quad + 5J_1^\alpha(\omega_0) + 2J_2^\alpha(2\omega_0)\}, \\ R_{21a}^\alpha &\equiv C^\alpha\{3[\omega_{q,\theta}^2 J_0^\alpha(0) + 2\omega_1^2(J_0^\alpha(0) + J_0^\alpha(k_1))]/k_1^2 \\ &\quad + J_1^\alpha(\omega_0) + 2J_2^\alpha(2\omega_0)\}, \\ R_{22a}^\alpha &\equiv C^\alpha[2J_1^\alpha(\omega_0) + 4J_2^\alpha(2\omega_0)]. \end{aligned} \tag{8}$$

In this case, $k_1 = \sqrt{\omega_{q,\theta}^2 + 4\omega_1^2}$, $C^\alpha \equiv \frac{3}{160}\chi_\alpha^2$, R^α is the coupling matrix, and σ_α is the related irreducible tensorial operator sets where the subscript α denotes a specific adsorption site, and $\chi_\alpha \equiv (e^2Qq_\alpha)/\hbar$ are the associated quadrupolar coupling constants. According to our previous study [5], there are two major types of water adsorption sites on the inner surface of MCM-41: slow motion sites and fast motion sites. The water in the slow motion sites is mainly bound water on the inner surface of MCM-41 which can be observed directly by DQF NMR due to residual quadrupolar interaction. According to Jacobsen et al. [6], the definitions of the spectral-density functions for slow motion site are given by

$$\begin{aligned} J_0^s(0) &= j_0(0)[1 + \tfrac{10}{7}\langle D_{00}^2\rangle + \tfrac{18}{7}\langle D_{00}^4\rangle - 5\langle D_{00}^2\rangle^2], \\ J_0^s(k_1) &= j_0(k_1)[1 + \tfrac{10}{7}\langle D_{00}^2\rangle + \tfrac{18}{7}\langle D_{00}^4\rangle - 5\langle D_{00}^2\rangle^2], \\ J_1^s(\omega_0) &= j_1(\omega_0)[1 + \tfrac{5}{7}\langle D_{00}^2\rangle - \tfrac{12}{7}\langle D_{00}^4\rangle], \\ J_1^s(2\omega_0) &= j_2(2\omega_0)[1 - \tfrac{10}{7}\langle D_{00}^2\rangle + \tfrac{3}{7}\langle D_{00}^4\rangle], \end{aligned} \tag{9}$$

where $j_m(\omega)$ ($m = 0$, 1, and 2) is the spectral density for the dynamic part of the molecular motion. The adsor-

bate dynamics in the slow motion sites modeled by the modified cone model of Brainard and Szabo [5,11] with two motion modes: the wobbling motion of the D_2O molecule along its C_2 and internal rotation motion of D_2O. The motional correlation times are defined by τ_w and τ_i, respectively. Thus the spectral density, $j_m(\omega)$, can be defined by

$$\begin{aligned} j_m(\omega) \equiv\, & 4S^2(d^2_{10}(\beta))^2 \frac{D_i}{D_i^2+(m\omega)^2} + 4S^2(d^2_{20}(\beta))^2 \frac{4D_i}{(4D_i)^2+(m\omega)^2} \\ & + 2(d^2_{00}(\beta))^2 \frac{(1-S^2)[6D_w/(1-S^2)]}{[6D_w/(1-S^2)]^2+(m\omega)^2} \\ & + 4(d^2_{10}(\beta))^2 \frac{(1-S^2)[D_i+5D_w/(1-S^2)]}{[D_i+5D_w/(1-S^2)]^2+(m\omega)^2} \\ & + 4(d^2_{20}(\beta))^2 \frac{(1-S^2)[4D_i+2D_w/(1-S^2)]}{[4D_i+2D_w/(1-S^2)]^2+(m\omega)^2}, \end{aligned} \tag{10}$$

where $D_i = 1/(4\tau_i)$ and $D_w = 1/(6\tau_w)$. $d^2_{nm}(\beta)$ are elements of the reduced Wigner rotation matrix and β is the fixed angle between the C_2 axis of D_2O molecule and principal axis of the residual quadrupolar interaction, i.e., the O–D direction. The distribution of orientations in the cone in the molecular frame is characterized by an order parameter, S ($0 \leqslant S \leqslant 1$). In the formulation, both S and ω_q are both subject to the same averaging process, thus, for convenience we define $S = \omega_q/\omega_{qm}$. S characterizes the strength of the residual interaction of the adsorbed water molecules. ω_{qm} is the maximum residual quadrupolar interaction for a D_2O molecule adsorbed on the adsorption site. For the D_2O quadrupolar interaction, $\omega_{qm} = \frac{3}{4}\chi s$, where χ_s is the quadrupolar coupling constant.

For the water molecules in the fast motion sites is mobile water in the pores of MCM-41 which the reorientational Brownian motion of water molecules averages the anisotropic quadrupole interaction experienced by the ^2H nucleus to zero, i.e., $\omega_{q,\theta} = 0$. Thus no double-quantum coherence (DQC) is generated in fast motion sites. The spectral-density function for fast motion site is given by

$$J^f_m = \frac{2\tau_c}{1+(m\omega_0\tau_c)^2}, \tag{11}$$

where τ_c is the effective reorientational correlation time of water molecules. Despite the signal from fast motion sites cannot be investigated directly, it still can be observed by DQF NMR indirectly due to the water being in exchange with water molecules in the slow motion site. Including the exchange process between the two sites, Eq. (7) becomes

$$\frac{\mathrm{d}}{\mathrm{d}t}\begin{bmatrix}\sigma_s \\ \sigma_f\end{bmatrix} = \begin{bmatrix} R^s - K_{sf} & K_{fs} \\ K_{sf} & R^f - K_{fs}\end{bmatrix}\begin{bmatrix}\sigma_s \\ \sigma_f\end{bmatrix}, \tag{12}$$

where $K_{\alpha\beta} \equiv k_{\alpha\beta}\mathbf{I}$ and $\mathbf{I}$ is the 4×4 identity matrix. The definitions of σ_s and σ_f follow those in Eq. (7) k_{fs} is the microscopic rate constant for transfer from fast motion sites to slow motion sites, and k_{sf} is the microscopic rate constant for transfer from slow motion sites to fast motion sites. The principle of detailed balance applied to the exchange process requires that $P_f k_{fs} = P_s k_{sf}$ where P_f and P_s denote the populations of spin-bearing molecules in the fast and slow motion sites, respectively. To guarantee the validity of Eq. (12), the condition $\tau_{ex} \gg \tau_c$ must hold, where τ_{ex} is defined as $\tau_{ex} \equiv P_s/k_{fs} = P_f/k_{sf}$.

Since we focus on the effects of the water adsorption dynamics on the $T_{2\rho}$ DQF spectrum, most parameters for simulating the $T_{2\rho}$ DQF spectral lineshapes were derived from conventional DQF and T_1 inversion-recovery spectral lineshape analysis [5]. Conventional and $T_{2\rho}$ DQF spectra were measured using the pulse sequences shown in Figs. 1A and B, respectively. The coherence-transfer pathways are described in Eq. (7). The applied spin-lock field transforms the Zeeman order T_{10} into double-quantum coherence $T_{22}(a)$ and then the $\pi/2$ pulse followed transfers double-quantum coherence into an observable signal. The other undesired coherences are canceled by the phase cycling.

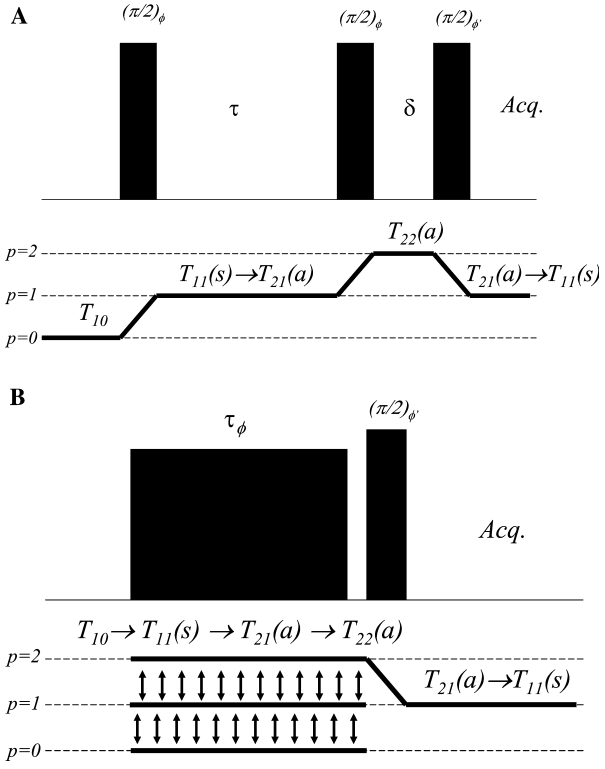

Fig. 1. The pulse sequence and coherence-transfer pathway for (A) DQF NMR. The phase cycles for the various components of the pulse sequence are as follows: $\phi = (X, Y, -X, -Y, X, Y, -X, -Y, X, Y, -X, -Y, X, Y, -X, Y)$ and $\phi' = (X, X, X, X\ Y, Y, Y, Y, -X, -X, -X, -X, -Y, -Y, -Y, -Y)$, and receiver phase, $\phi_R = (X, -X, X, -X, -Y, Y, -Y, Y, -X, X, -X, X, Y, -Y, Y, -Y)$. (B) $T_{2\rho}$ DQF NMR. $\phi = (X, Y, -X, -Y, X, Y, -X, -Y, X, Y, -X, -Y, X, Y, -X, -Y, X, Y, -X, Y)$ and $\phi' = (X, X, X, X, Y, Y, Y, Y, -X, -X, -X, -X, -Y, -Y, -Y, -Y)$, and receiver phase, $\phi_R = (X, -X, X, -X, -Y, Y, -Y, Y, -X, X, -X, X, Y, -Y, Y, -Y)$.

As noted above, the $T_{2\rho}$ DQF NMR sequence mainly reports on the water signal from slow motion sites. Whereas the single quantum (SQ) signals observed in the inversion-recovery experiment report on the water signal from both the slow and fast motion sites [5]. Hence the motional parameters determined from both $T_{2\rho}$ DQF NMR and inversion-recovery experiments must be self-consistent.

3. Experimental

3.1. Sample preparation

Cetyltrimethylammonium bromide (CTAB) (99%; Acrōs) was dissolved in deionized water at 308 K while stirring. A solution of sodium silicate (Aldrich, 14% NaOH and 27% SiO_2), was added and the resulting gel was stirred for 20 min. The pH of the gel was adjusted to 10 with 1.2 M sulfuric acid (Acrōs). The molar composition of the gel was 1.00 SiO_2:0.35 CTAB:0.28 H_2SO_4:100 H_2O. The gel was then stirred for a further 1 h before being transferred to a Teflon-lined autoclave where it was heated at 373 K for 48 h. The final solid product obtained after filtration, was washed with deionized water, dried in air at room temperature, and calcined at 833 K for 6 h.

X-ray powder diffraction data of the MCM-41 was collected on a Scientag XI diffractometer using CuK_α radiation. The average pore diameter was estimated from the d_{100}-spacing of the X-ray diffractograms. The surface-area and pore-size measurements were performed on a homemade high vacuum system. The sample was degassed at 590 K and 1 mPa for 16 h. Assuming the thickness of the walls to be 1 nm, the estimated average pore diameter was 3.38 ± 0.17 nm. The sample has BET surface areas of 900 ± 45 m^2 g^{-1}, which is characteristic of mesoporous materials.

The MCM-41 was initially dried under a vacuum of 10^{-5} torr at 650 K for more than 16 h and then transferred to an 8 mm ID tube approximately 40 mm long. Two samples with deuterated water loadings of 11.1 and 4.8% (w/w%) were prepared. From our previous DQF NMR and inversion-recovery measurements [5], the water distributions in MCM-41 in these two samples were known to be different. Water is distributed in both the slow and fast motion sites in the 11.1% D_2O loaded sample and, as expected, it gives a better S/N ratio than the 4.8% D_2O loaded sample and this sample was mainly utilized in the investigation of trend of intensity variation for saving time. Since the 4.8% D_2O loaded sample has only water in the slow motion site, its DQ signals are much simpler. Then, the sample tubes were sealed and kept at 373 K for at least 24 h to ensure a homogeneous distribution of adsorbate in the sample before the NMR measurement.

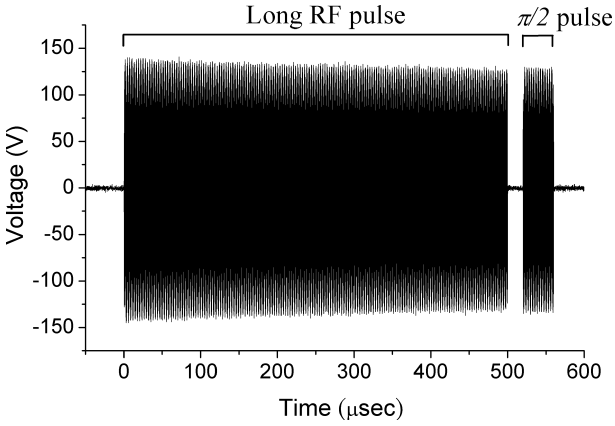

Fig. 2. The RF profile of the $T_{2\rho}$ DQF NMR pulse sequence (see Fig. 1B) monitored using an oscilloscope. The RF pulse profile is distorted due to the duty cycling limitation of the RF transmitter.

3.2. NMR measurement

The ^2H NMR measurements were performed on Bruker MSL-500 spectrometer operating at 76.78 MHz (11.75 T) with a 90° pulse of 16 μs. The receiver recovery time is less than 10 μs, and the probe dead time is 10 μs. Typical acquisition parameters were a spectral width of 125 kHz digitized into 8K data points. Each spectrum was the result of averaging 10,000 scans. A delay of at least 5 T_1 was allowed between scans for the T_1, DQF, and $T_{2\rho}$ DQF NMR spectra. The temperature was controlled to a precision of ±0.1K and was calibrated using methanol. The magnetic inhomogeneity was estimated by comparing Hahn spin-echo and linewidth measurements and was found to account for less than 5 Hz of the observed linewidth at half height. The longitudinal relaxation measurements were obtained using the inversion-recovery pulse sequence. For the $T_{2\rho}$ DQF NMR, the RF pulse profile was monitored and recorded by a Tektronix TDS 3032B oscilloscope. In Fig. 2, the long-RF pulse profile is distorted due to the duty cycling limitation of the RF transmitter. All NMR measurements reported here were performed within 1 month of sample preparation. However the longitudinal relaxation behavior was observed to be constant over a period of 2 months—indicating that equilibrium had been reached in the pore systems prior to the initiation of the NMR measurements.

4. Results and discussion

To investigate the characteristic features of the $T_{2\rho}$ DQF NMR spectra, the $T_{2\rho}$ DQF NMR spectra of the 11.1% D_2O loaded sample at 273 K are exhibited in Fig. 3A and for comparison the conventional DQF NMR spectra are presented in Fig. 3B. The $T_{2\rho}$ DQF NMR spectral intensity oscillates with the double

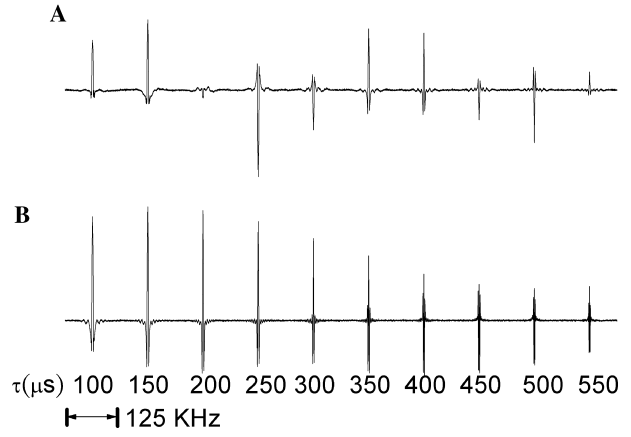

Fig. 3. (A) $T_{2\rho}$ DQF and (B) conventional DQF NMR spectra of the 11.1% D_2O loaded sample for various DQ evolution times at 273 K.

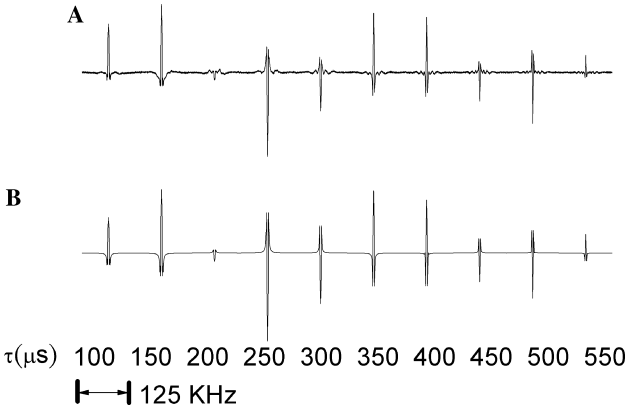

Fig. 4. (A) $T_{2\rho}$ DQF spectra and (B) simulations of the 11.1% D_2O loaded sample for various DQ evolution times at 273 K. The parameters used in the simulations are tabulated in Table 1.

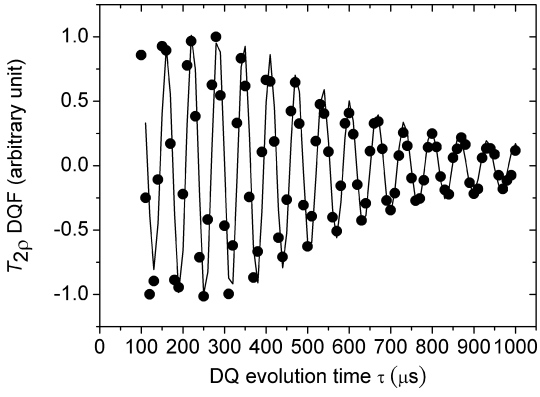

Fig. 5. The change in intensity of the $T_{2\rho}$ DQF NMR spectra with DQ evolution time of the 11.1% D_2O loaded sample at 295 K. Solid circles (●) represent the $T_{2\rho}$ DQF NMR peak intensity data and the solid curve is the theoretical calculation.

quantum evolution time, τ, while the conventional DQF NMR spectra show monotonic decay with τ. To clarify the origin of the oscillation in the $T_{2\rho}$ DQF NMR spectrum, the experimental spectrum of the 11.1% loaded sample at 273 K was compared with a theoretical simulation (see Fig. 4). And in Fig. 5, the oscillation of the $T_{2\rho}$ DQF NMR spectral intensity of the 11.1% sample at 295 K with 10 μs increments of the DQ evolution time is presented together with the simulated results. Excellent agreement was obtained between the experimental and simulated results and the parameters used in the theoretical calculations are tabulated in Table 1.

$T_{21}(a)$ and $T_{22}(a)$ are coupled to each other by the RF field via the ω_1 term as shown in Eq. (7). The DQC, $T_{22}(a)$, oscillates approximately following $\sin(\omega_1 t)$, that is, the period of oscillation of the $T_{2\rho}$ DQF NMR signals is proportional to the amplitude of the RF field. As can be understood from Fig. 2, as τ increases, the RF field strength decreases. And as shown in Fig. 5 the oscillation period increases from 60 to 70 μs with increasing τ. The B_1-dependence of the oscillation frequency provides a means for determining the RF strength, including the effects of the amplitude decrease with increasing RF duty cycle, for use in the simulations.

In addition to the effect of RF field, the residual quadrupolar interaction also has unique influences on the $T_{2\rho}$ DQF NMR spectra. To investigate the effect of residual quadrupolar interaction, the 4.8% loaded sample was so as to minimize the effect of water exchange. The DQF NMR and $T_{2\rho}$ DQF NMR spectra of the 4.8% D_2O loaded sample in the temperature range from 220 to 273 K is shown in Fig. 6. The $T_{2\rho}$ DQF NMR intensity profile shows temperature-dependent damped oscillations and phase variation. The $T_{2\rho}$ DQF NMR spectral intensity profiles is clearly more sensitive to temperature than that of conventional DQF NMR.

Experimental and simulated $T_{2\rho}$ DQF spectral intensity profiles of the 4.8% loaded sample in the temperature range of 220–273 K are shown in Fig. 7. The simulation parameters are tabulated in Table 2. From the lineshape analysis of the conventional DQF NMR and inversion-recovery experiments for the 4.8% D_2O loaded sample, it was inferred that only slow-site water molecules exist. Hence, the effects of exchange were neglected when simulating the results from this sample. The agreement between experimental and theoretical simulation shows that the variation of intensity profiles

Table 1
Parameters used in simulation for 11.1% D_2O contained sample

Temperature (K)	P_f/P_s	τ_c^{fi} (s)	τ_w (s)	τ_i (s)	τ_{ex}^{fis} (s)	S
295	0.3	$1.0 \pm 0.5 \times 10^{-11}$	$6.0 \pm 0.2 \times 10^{-5}$	$3.0 \pm 0.1 \times 10^{-11}$	$4.0 \pm 0.1 \times 10^{-4}$	0.023 ± 0.001
273	0.29	$1.0 \pm 0.5 \times 10^{-11}$	$1.0 \pm 0.1 \times 10^{-5}$	$4.5 \pm 0.1 \times 10^{-11}$	$9.0 \pm 0.1 \times 10^{-4}$	0.024 ± 0.001

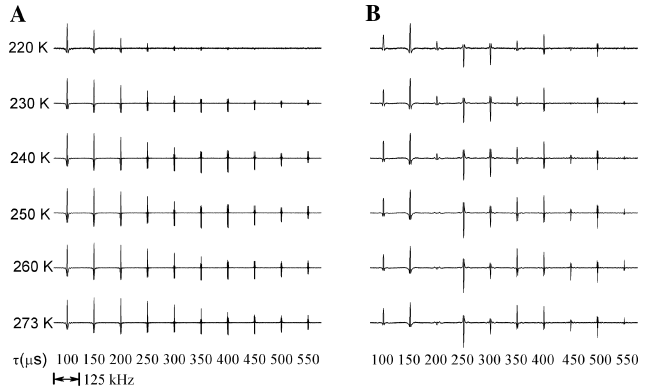

Fig. 6. (A) Conventional DQF NMR and (B) $T_{2\rho}$ DQF NMR spectra for the 4.8% D_2O loaded sample at various values of the DQ evolution time in the temperature range from 220 to 273 K.

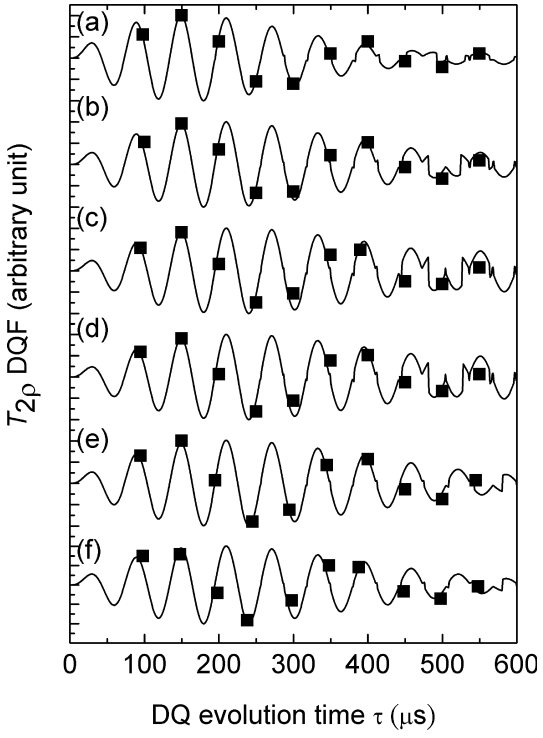

Fig. 7. $T_{2\rho}$ DQF NMR spectral intensity profile for the 4.8% D_2O loaded sample at: (a) 220 K, (b) 230 K, (c) 240 K, (d) 250 K, (e) 260 K, and (f) 273 K. Solid rectangles (■) represent the peak intensity of the $T_{2\rho}$ DQF NMR spectra. The solid curves are the theoretical simulation.

Table 2
Parameters used in simulation for 4.8% D_2O contained sample

Temperature (K)	τ_w (s)	τ_i^s (s)	S
220	$8.0 \pm 0.5 \times 10^{-5}$	$9.5 \pm 0.5 \times 10^{-11}$	0.030 ± 0.001
230	$4.5 \pm 0.6 \times 10^{-5}$	$7.0 \pm 0.4 \times 10^{-11}$	0.030 ± 0.001
240	$2.5 \pm 0.1 \times 10^{-5}$	$6.5 \pm 0.3 \times 10^{-11}$	0.030 ± 0.001
250	$2.3 \pm 0.1 \times 10^{-5}$	$6.5 \pm 0.2 \times 10^{-11}$	0.030 ± 0.001
260	$2.3 \pm 0.1 \times 10^{-5}$	$5.0 \pm 0.1 \times 10^{-11}$	0.026 ± 0.001
273	$2.3 \pm 0.2 \times 10^{-5}$	$2.0 \pm 0.1 \times 10^{-11}$	0.026 ± 0.001

with temperature mainly results from the wobbling motion and the distribution of the adsorbate which is characterized by the order parameter [5]. The values of the order parameters tabulated in Table 2 show that the water molecules become more ordered at lower temperatures, and as a consequence there is a stronger residual quadrupolar interaction as well. The rugged features that appear around $\tau = 500$ μs in the calculated curves in Fig. 7 provide direct evidence of the variation of the residual quadrupolar interaction with temperature. As mentioned above, the residual quadrupolar interaction coupling may account for an extra oscillation of the form of $\sin(\omega_{q,\theta}t)$ in addition to the effect of the RF field. Using Eq. (7) and the time at which the rugosity appeared it was possible to estimate the residual quadrupolar interaction (i.e., $\omega_{q,\theta}$) to be around 4 kHz. This value roughly equals the splitting of the SQ spectra found in the temperature range 220–273 K. To verify the periodic behavior of the rugosity, Fig. 8 demonstrates the theoretical calculations of the spectral intensity profiles for the 11.1 and 4.8% D_2O loaded samples. The result in Fig. 8B obviously shows the rugosity with a period of ~500 μs. Therefore, the τ value at which rugosity appears is thus an indicator of the strength of the residual quadrupolar interaction of the water in MCM-41. Since the strength of the

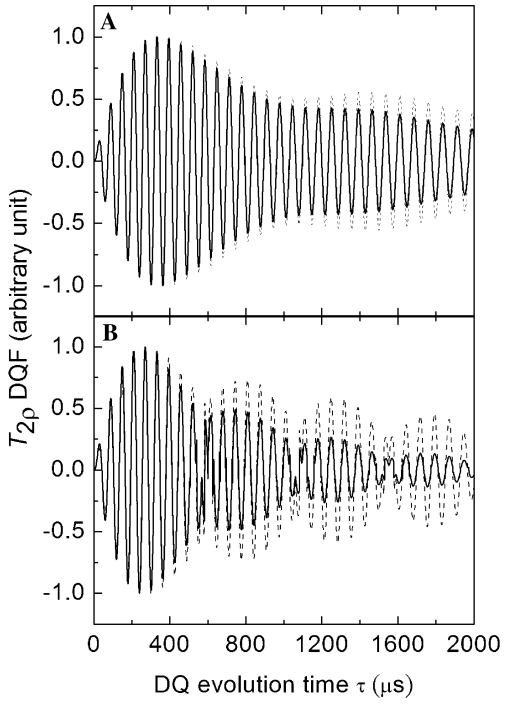

Fig. 8. The theoretical simulations of the spectral intensity profiles for (A) the 11.1% and (B) 4.8% D_2O loaded samples at 273 K. The solid curves are simulations including the effects of the RF field, residual interaction, and electric quadrupolar relaxation. The simulations represented by the dashed curves neglect relaxation effects during DQ evolution period.

residual quadrupolar interaction increases with decreasing temperature the rugosity appears at progressively shorter τ values as shown in Fig. 7.

To clarify the effect of the exchange process on $T_{2\rho}$ DQF NMR, the experimental spectral intensity profiles for the 11.1 and 4.8% D_2O loaded samples at 273 K and the corresponding theoretical simulations (both with and without the effects of relaxation; see Eq. (7) are compared in Fig. 8. The simulation parameters are tabulated in Tables 1 and 2. Clearly the $T_{22}(a)$ term remains constant in the absence of RF irradiation. Comparison of Figs. 8A and B reveals that the exchange between the slow and fast motion sites enhances the signal decay, but the RF field and residual quadrupolar interactions are nevertheless the dominant factors in determining the intensity decay during the DQ evolution period. The node that appears around 500–600 μs in Fig. 8B is due to the interference of $T_{11}(s)$ and $T_{21}(a)$ via the residual quadrupolar interaction. Vega and Pines [2] demonstrated a similar effect by using different combinations of RF fields and quadrupolar interaction strengths. However, as they used a short RF field duration (60 μs) they did not demonstrate the decay of the coherences.

To clarify the detailed time evolution of the coherence transfer more precisely, the effects of the coupling of the terms were investigated with the 4.8% D_2O loaded sample. As shown in Fig. 9, T_{10} and $T_{11}(s)$ are dominant initially due to their coupling by the RF field. The effects of $T_{21}(a)$ and $T_{22}(a)$ start to appear around $\tau = 200$ μs and have their maximum value at around 300–400 μs. $T_{21}(a)$ is generated mainly due to the residual quadrupolar interaction and later the coupling of the RF field with $T_{22}(a)$. In the present studies, the RF field strength is much stronger than the other coupling interactions.

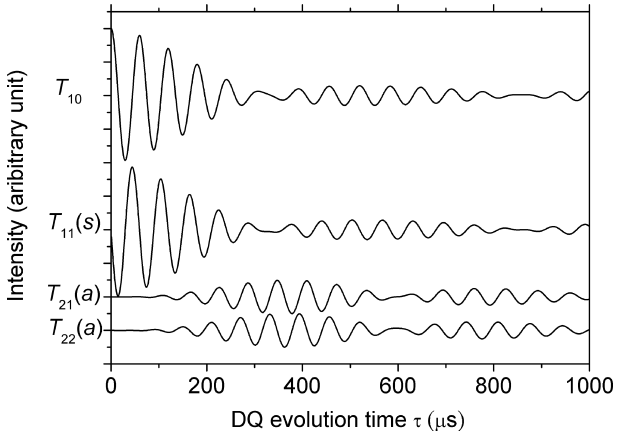

Fig. 9. The time evolution of the various spin coherences at 273 K. The traces are normalized to the initial intensity of T_{10} and have been offset to allow easy visualization. The parameters used for simulations are those tabulated in Table 2.

By examining the evolution of each component, as shown in Fig. 9, it is observed that the decreasing of the SQ coherences is correlated with an increase of the $T_{21}(a)$ and $T_{22}(a)$ coherences during the periods $\tau = 200$–400 μs and 800–1000 μs. By judicious choice of DQ evolution time, DQC or SQC can be selectively enhanced. Further, the coupling RF field can lead to decays of individual coherences. The decay pathway can be considered as a re-distribution process even in the absence of the influence of spin relaxation—an entropic effect for magnetization within a given coupling scheme.

In addition to the present application, the effect of long-duration RF irradiation is especially important in MRI due to the prevalence of soft pulses in MRI sequences. During such long-RF pulses, coupling through other interactions, such as the residual dipolar interaction, may create the multi-quantum coherences as observed in this study. Specially designed soft RF pulses may provide an alternative means for generating multi-quantum coherences in intermolecular and intramolecular dipolar interaction systems. This work may lead to the design of simple pulse sequences for MQ imaging. We are presently developing sophisticated $T_{2\rho}$ DQF NMR-based MRI techniques in our laboratory.

5. Conclusions

We have experimentally and theoretically demonstrated the creation of multi-quantum coherences in spin systems coupled with the residual dipolar interaction during long-duration RF pulses. The results have special significance for the development of multi-quantum MRI techniques.

Acknowledgments

This work was supported by the National Science Council of the Republic of China under Grant No. NSC 92-2113-M-001-038 and Ministry of Education of the Republic of China under Grant No. A-91-N-FA01-2-4-3.

References

[1] J.S. Blicharski, Nuclear magnetic relaxation in the rotating frame, Acta Phys. Polon. A 41 (1972) 223–236.
[2] S. Vega, A. Pines, Operator formalism for double quantum NMR, J. Chem. Phys. 66 (1977) 5624–5644.
[3] Y.H. Chen, L.P. Hwang, Investigation of the benzene molecule adsorbed on faujasite zeolite using double quantum filtered NMR spectral analysis, J. Phys. Chem. B 103 (1999) 5070–5080.
[4] T.Y. Yu, C.Y. Cheng, D.W. Hwang, L.P. Hwang, Water-filled MCM-41 characterized by double-quantum-filtered ^2H NMR spectral analysis, Appl. Magn. Reson 18 (2000) 435–453.

[5] D.W. Hwang, A.K. Sinha, C.Y. Cheng, T.Y. Yu, L.P. Hwang, Water dynamics on the surface of MCM-41 via ^{2}H double quantum filtered NMR and relaxation measurements, J. Phys. Chem. B 105 (2001) 5713–5721.

[6] J.P. Jacobsen, H.K. Bildsoe, K. Schaumburg, Application of density matrix formalism in NMR spectroscopy. II. The one-spin-1 case in anisotropic phase, J. Magn. Reson. 23 (1976) 153–164, There are some misprints in Eq. (32). The coefficient of $\langle D^2_{00}\rangle$ in $J_0(0)$ and $J_2(2\omega_r)$ should be corrected as -5 and 10/7 instead of -1 and $5\sqrt{2/7}$ as printed, respectively.

[7] J.R.C. vander Maarel, The relaxation dynamics of spin $I = 1$ nuclei with a static quadrupolar coupling and a radio-frequency field, J. Chem. Phys. 99 (1993) 5646–5653.

[8] L. Tsoref, H. Shinar, Y. Seo, U. Eliav, G. Navon, Proton double-quantum filtered MRI—a new method for imaging ordered tissues, Magn. Reson. Med. 40 (1998) 720–726.

[9] W.S. Warren, S. Ahn, M. Mescher, M. Garwood, K. Ugurbil, W. Richter, R.R. Rizi, J. Hopkins, J.S. Leigh, MR imaging contrast enhancement based on intermolecular zero quantum coherences, Science 281 (1998) 247–251.

[10] G.J. Bowden, W.D. Hutchison, Tensor operator formalism for mulit-quantum NMR. 1. Spin-1 nuclei, J. Magn. Reson. 67 (1986) 403–414.

[11] J.R. Brainard, A. Szabo, Theory for nuclear magnetic relaxation of probes in anisotropic systems: application to cholesterol in phospholipid vesicles, Biochemistry 20 (1981) 4618–4628.